Instability of surface temperature filaments in strain and shear

B. J. Harvey and M. H. P. Ambaum

Department of Meteorology, University of Reading, UK

Abstract

The effects of uniform straining and shearing on the stability of a surface quasi-geostrophic temperature filament are investigated. Straining is shown to stabilise perturbations on wide filaments but only for the finite time until the filament thins to a critical width, after which some perturbations can grow. No filament can be stabilised in practice since there are perturbations which can grow large for any strain rate. The optimally growing perturbations, defined as solutions which reach a certain threshold amplitude first, are found numerically for a wide range of parameter values. The radii of the vortices formed through non-linear roll-up are found to be proportional to θ/s, where θ is the temperature anomaly of the filament and s the strain rate, and not dependent on the initial size of the filament.

Shearing is shown to reduce the normal mode growth rates but cannot stabilise them completely when there are temperature discontinuities in the basic state; smooth filaments can be stabilised completely by shearing and a simple scaling argument provides the shear rate required.

1 Introduction

The surface quasi-geostrophic (SQG) equations provide an accurate model for the motion of rapidly rotating stratified fluids near horizontal boundaries. In the atmospheric context there

is a body of work applying the SQG equations to the dynamics of surface temperature anomalies (Müller et al. (1989), Schär & Davies (1990), Ambaum & Athanasiadis (2007)) and also to the dynamics of tropopause height anomalies (Juckes (1994), Juckes (1995), Juckes (1999), Tulloch & Smith (2006)). More recently their application to upper-level ocean dynamics has also been demonstrated (Lapeyre & Klein (2006)).

The model consists of 2-dimensional advection of the boundary temperature field under the assumption of uniform potential vorticity in the fluid interior. The surface streamfunction is related to the surface temperature field by a Green's function which decays like $1/r$, see (4). This induces a more localised dynamics compared to the more familiar barotropic vorticity equation which has a Green's function with a $-\log r$ decay. The $1/r$ Green's function is the same as the full 3-dimensional quasi-geostrophic flow and the SQG system does exhibit flavours of 3-dimensional flows despite its 2-dimensional form (Constantin et al. (1994)).

Here we investigate the striking 'curdling' at small scales which is apparent in many SQG turbulence simulations (Pierrehumbert et al. (1994), Held et al. (1995), Juckes (1995)). This curdling is an explanation for the instability of filamentary stratospheric intrusions as well as surface temperature features. The production and stretching of filamentary structures is a ubiquitous feature of 2-dimensional fluid flows, providing a mechanism for the transport of enstrophy to small scales. In the SQG case, however, the filaments appear prone to instability leading to their break up and the subsequent formation of smaller scale vortices. These vortices in turn shed smaller filaments themselves and the process repeats to ever smaller scales. The smaller scale SQG filaments have larger perturbation growth rates, see below, and therefore this process can potentially accelerate, resulting in intense activity at small scales on very short time scales, hence the curdling.

The stability of an isolated SQG temperature filament was studied in detail by Juckes (1995). In this paper we investigate the filament instability under typical turbulence condi-

tions by considering separately the effects of external straining and shearing flows. Such flows provide a first order approximation to the general tendency of the large scale components of flows to form, stretch, thin and shear smaller scale filamentary structures.

That external flows can strongly affect fluid dynamic instabilities has long been understood. Dritschel (1989) and Dritschel et al. (1991) study the most basic cases of a barotropic vorticity filament in shear and strain respectively, and we follow a similar methodology in this study. They find that suitably strong shear or strain can completely stabilise vorticity filaments. Other studies have subsequently applied these ideas to the stability of frontal potential vorticity anomalies in the atmosphere (e.g. Dacre & Gray (2006), Bishop & Thorpe (1994)).

Because the SQG system is less familiar than the barotropic system we briefly outline its structure and the notation we employ in Section 2. We then review the basic instability mechanism of SQG filaments in the absence of external flow fields in Section 3. The analysis of the straining case is presented in Sections 4-6. In Section 4 we consider the instantaneous growth rates of perturbations analytically, in Section 5 we present numerical integrations of the initial value problem to study the evolution of perturbations in detail. Finally in Section 6 we consider an alternative approach to the initial value problem whereby we suppose perturbations are continually applied to the filament since, as we show, the first perturbation to be applied is not always the first to become large. The analysis of the shear case is more straightforward and is presented in Section 7. We present some concluding remarks in Section 8.

2 Governing equations

With the atmospheric surface temperature anomaly application in mind for the choice of notation, we write the SQG system as follows.

$$\frac{D\theta}{Dt} = 0 \quad \text{at} \quad z = 0 \tag{1}$$

$$\text{and} \quad \nabla^2\psi = 0 \quad \text{in} \quad z > 0, \tag{2}$$

where θ is proportional to the potential temperature anomaly and ψ is the geostrophic stream-function, $D/Dt = \partial/\partial t + u\partial/\partial x + v\partial/\partial y$ is the geostrophic Lagrangian derivative and (2) represents the condition of zero interior PV. The geostrophic variables are given by

$$(u, v, \theta) = (-\psi_y, \psi_x, \psi_z) \tag{3}$$

and u, v and θ are all assumed to decay at large z. Given a surface θ distribution, (2)-(3) then determine all other fields uniquely. For the atmospheric lower boundary application, θ is the potential temperature anomaly scaled by $g/\theta_{00}N$ and therefore has the dimension of a velocity field, z is the vertical coordinate scaled with the Prandtl ratio, N/f, and θ_{00} is a constant background reference temperature.

In the following we suppress the z-dependence of all variables and consider only their surface values. The inversion of a surface temperature distribution $\theta(\mathbf{x})$, where $\mathbf{x} = (x, y)$, then takes the form

$$(u, v)(\mathbf{x}) = -\frac{1}{2\pi}\left(-\frac{\partial}{\partial y}, \frac{\partial}{\partial x}\right)\int\int \frac{\theta(\mathbf{x}')}{|\mathbf{x} - \mathbf{x}'|}\, d^2\mathbf{x}', \tag{4}$$

which can be derived by considering the Fourier transform of the full 3-dimensional system. For a 1-dimensional surface temperature profile $\theta = \theta(y)$ this inversion reduces to a Hilbert transform,

$$u(y) = -\frac{1}{\pi}\int_{-\infty}^{\infty} \frac{\theta(y')}{y - y'}\, dy', \quad v = 0. \tag{5}$$

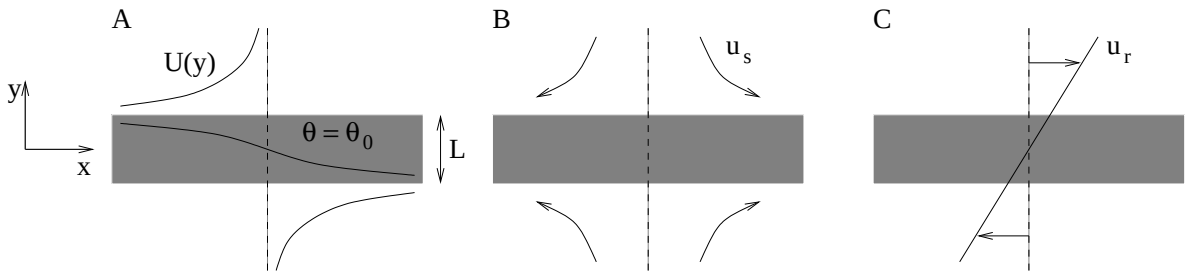

Figure 1: Sketches of the basic state temperature and velocity fields (A), the strain flow of Equation (20) (B) and the shear flow of Section 7 (C).

3 Analysis of an isolated filament

Here we briefly outline the stability analysis of an SQG filament in a quiescent background flow. Many of the results were derived by Juckes (1995); the purpose of this review is to introduce notation and define several important parameters used in later sections.

The problem considered is that of a filament of anomalous surface temperature with a 'top-hat' profile as illustrated in Figure 1A,

$$\theta = \Theta(y) \equiv \begin{cases} \theta_0 & \text{for} \quad |y| < L/2 \\ 0 & \text{for} \quad |y| > L/2. \end{cases} \tag{6}$$

The velocity field induced by this temperature anomaly is also sketched in the figure. By (5), it is proportional to the Hilbert transform of the temperature field,

$$u = U(y) = \frac{\theta_0}{\pi} \log \left| \frac{y - L/2}{y + L/2} \right|, \quad v = 0. \tag{7}$$

The logarithmic singularities in the velocity field along the edges of the filament are a generic feature of temperature discontinuities under SQG inversion (see Held et al. (1995)). Juckes (1995) shows that despite this singularity the stability characteristics of a slightly smoothed version of this filament are regular in the limit of sharp edges, at least for wave numbers $k \ll \delta L^{-1}$ where δL is the width of the smoothing. We concentrate on the sharp edge case in the following.

In the sharp edge limit, the dynamics are governed entirely by the positions of the filament edges. Suppose the edges are perturbed to the new positions $y_1(x,t) = (1/2 + \epsilon\eta_1(x,t))L$ and $y_2(x,t) = (-1/2 + \epsilon\eta_2(x,t))L$ where ϵ is a small non-dimensional parameter. Conservation of θ requires the filament edges to be material lines and so their evolution is given by

$$\frac{\partial \eta_1}{\partial t} = \mathbf{u}(x, y_1 + \delta) \cdot \left(-\frac{\partial \eta_1}{\partial x}, \frac{1}{\varepsilon L} \right)^T \tag{8}$$

$$\frac{\partial \eta_2}{\partial t} = \mathbf{u}(x, y_2 + \delta) \cdot \left(-\frac{\partial \eta_2}{\partial x}, \frac{1}{\varepsilon L} \right)^T \tag{9}$$

in the limit $\delta \to 0$. These equations represent the advection of the boundary by the velocity field at the positions $y = y_1 + \delta$ and $y = y_2 + \delta$ respectively. At these locations the velocity field is finite. In the limit $\delta \to 0$ the velocity components become large, but the inner products remain finite: the large velocities always run parallel to the edges, leaving evolution of the temperature field on finite time scales. For a more detailed discussion see Held et al. (1995), Juckes (1995) and **?**.

Juckes (1995) simplifies the system (8)-(9) by linearising the velocity field for small ϵ. The dynamics of perturbations on each edge of the filament then consist of a contribution from self-propagation and a contribution from interaction with the opposite edge, a process which can be written succinctly in terms of Fourier components:

$$i\frac{d\hat{\boldsymbol{\eta}}}{dt} = \begin{pmatrix} P(\kappa) & I(\kappa) \\ -I(\kappa) & -P(\kappa) \end{pmatrix} \hat{\boldsymbol{\eta}} \equiv \mathcal{F}\hat{\boldsymbol{\eta}}, \tag{10}$$

where

$$\kappa = kL \tag{11}$$

is the non-dimensional wavenumber and the Fourier components of the disturbance are defined by $(\eta_1, \eta_2) = \hat{\boldsymbol{\eta}}(t)e^{ikx}$. The propagation ($P$) and interaction ($I$) coefficients for the SQG

filament problem are given by

$$P(\kappa) = \frac{\theta_0}{\pi L}\kappa(\log\kappa + \gamma - \log 2) \tag{12}$$

$$I(\kappa) = \frac{\theta_0}{\pi L}\kappa \mathrm{K}_0(\kappa) \tag{13}$$

where $\gamma = 0.57721...$ is the Euler constant and K_0 is the modified Bessel function of order zero.

The general solution to (10) can be written as

$$\hat{\boldsymbol{\eta}}(t) = (\mathcal{I}\cosh\sigma t - \mathcal{F}\frac{i\sinh\sigma t}{\sigma})\hat{\boldsymbol{\eta}}(0) \tag{14}$$

where $\sigma = \sqrt{\det\mathcal{F}} = \sqrt{I^2 - P^2}$ is the normal mode growth rate and $\mathcal{I}$ is the identity matrix. Note from (12) and (13) that $\sigma \propto \theta_0/L$ in the SQG case and so perturbation growth rates are inversely proportional to the filament width.

To measure the amplification of disturbances we use the r.m.s. wave slope norm which, for a single Fourier mode, is given by

$$\mathcal{N}(t) = \frac{\kappa}{\sqrt{2}}\left|\hat{\boldsymbol{\eta}}(t)\right|. \tag{15}$$

This norm represents the size of the dominant nonlinear terms in the governing equations, which typically consist of derivatives, and as such is a useful diagnostic for nonlinear development (Dritschel et al. (1991)). The corresponding norm amplification factor is (taking $|\hat{\boldsymbol{\eta}}(0)| = 1$)

$$\mathcal{A}(t) \equiv \frac{\mathcal{N}(t)}{\mathcal{N}(0)} = \left|\hat{\boldsymbol{\eta}}(t)\right|, \tag{16}$$

the rate of change of which can be shown to be given by

$$\frac{d\mathcal{A}}{dt} = -\frac{2}{|\hat{\boldsymbol{\eta}}|}I(\kappa)\mathrm{Im}(\hat{\eta}_1\hat{\eta}_2^*), \tag{17}$$

where $\mathrm{Im}(\cdot)$ represents the imaginary component of the argument. This growth rate takes a maximal value of $I(\kappa)$ for waves of equal amplitude and a phase difference of $\pi/2$. This

is therefore the disturbance configuration which undergoes maximum instantaneous growth under this norm.

Two further quantities of interest are the value of the amplification factor (16) maximised over all initial conditions of a given wavenumber,

$$\mathcal{A}^*(t) \equiv \max_{\hat{\boldsymbol{\eta}}(0)}(\mathcal{A}(t)), \tag{18}$$

and the corresponding equivalent growth rate

$$\sigma^*_{eq} = \log(\mathcal{A}^*(t))/t. \tag{19}$$

Initially (when $\sigma t \ll 1$), $\sigma^*_{eq} \sim I(\kappa)$ and in the long time limit (when $\sigma t \gg 1$), $\sigma^*_{eq} \sim \sigma$: the equivalent growth rate collapses onto the normal mode growth rate in the long time limit. This represents the possibility of transient growth at a rate larger than σ initially followed by what is effectively normal mode growth. A full explanation of this process is given by Juckes (1995) who plots σ^*_{eq}, see Figure 2b of that study. We have also reproduced the plot in Figure 8 to allow easy comparison with our shearing case of Section 7.

4 External strain

We now investigate the effects of an external strain on this stability problem. We will demonstrate that the straining is a stabilising process in the sense that all linear perturbations eventually decay when there is an external strain present. However, we will also show that at intermediate times perturbation growth to any specified amplitude can occur. In this sense, the SQG filament cannot be stabilised by strain.

The external strain is written as

$$(u_s, v_s) = s(x, -y), \tag{20}$$

where s is the strain rate. The effect of this flow on the basic state of (6) is to thin the filament exponentially in the y-direction so that at later times its width is given by $L = L_0 e^{-st}$,

where L_0 is the width of the filament at $t = 0$. Note that this increases the growth rate of perturbations in the absence of straining which, from (12) and (13), is proportional to θ_0/L.

The straining also has a direct effect on perturbations which are squashed in the y-direction and stretched in the x-direction. The linear evolution is still given by (10) but now with time-varying wave numbers, $k = k_0 e^{-st}$, which correspond to

$$\kappa = \kappa_0 e^{-2st}, \tag{21}$$

and the wave slope norm of (16) becomes

$$\mathcal{A}(t) = e^{-2st}|\hat{\boldsymbol{\eta}}|. \tag{22}$$

where $\hat{\boldsymbol{\eta}}$ are the Fourier components of both edge perturbations.

We thus see that the strain introduces two competing effects: there is a kinematic decay of perturbations at the constant rate $2s$, which is stabilising, whilst the thinning of the filament causes an exponential increase in the instantaneous perturbation growth rates.

The analytic solution of (14) is not valid for non-zero strain rates so in Sections 5 and 6 we resort to numerical integration to analyse the problem in detail. As a first consideration of the combined effects, however, consider the instantaneous growth rates of perturbations for which there is a simple analytic result. From (17) and (22) it is clear that the rate of change of $\mathcal{A}$ takes a maximum value of $I(\kappa) - 2s$ when there is straining, and therefore for each strain rate there is a critical filament width above which no perturbations can grow,

$$L = L_c = \max_{\kappa} \left(\frac{\kappa \mathrm{K}_0(\kappa)}{2\pi} \right) \frac{\theta_0}{s} \equiv C \frac{\theta_0}{s}, \tag{23}$$

where $C \approx 0.0742$. This maximum value is achieved at non-dimensional wavenumber $\kappa \approx 0.595$. Note also that in the long time limit, whereby $\kappa \to 0$, all perturbations will decay at the kinematic rate of $-2s$.

The result of (23) suggests two regimes for the filament. Either $L < L_c$ initially and there are some perturbations which can grow, or else $L > L_c$ initially and all perturbations initially

decay. At the later time

$$t = t_c = \frac{1}{s} \log \left(\frac{sL_0}{C\theta_0} \right), \tag{24}$$

where L_0 is the initial filament width, there will be some perturbations which can grow. Therefore instantaneous perturbation growth can occur for any strain rate but only after the filament has thinned to the critical width L_c.

Applying this argument to the initial value problem, which we study in detail in Section 5, we note that the amplitude of a perturbation applied to a wide filament, in the sense that initially $L > L_{\rm c}$, will have decayed kinematically by the time $t = t_{\rm c}$ and will therefore be smaller at this time than its initial value. Whether the perturbation can subsequently become large will depend on whether the ensuing period of growth is sufficient to overcome the initial decay. Note also that if the filament was perturbed with a further disturbance of amplitude $\mathcal{A} = 1$ at time $t = t_{\rm c}$ then this new disturbance will possibly grow large before the initial perturbation does because it will not have undergone the initial decay. We consider this alternative to the initial value problem in Section 6.

Finally, we briefly note the similarity of the result (23) with that of Dritschel et al. (1991) for the barotropic vorticity case who found that perturbation growth on vorticity filaments is prevented if $s > 0.25q_0$, where q_0 is the filament vorticity. Likewise, the condition of (23) means that perturbation growth in the SQG case is prevented if $s > C\theta_0/L$. The difference here is the factor L which, due to the exponential thinning of the filament, means that the condition cannot be met indefinitely.

5 Initial value problem

We scale time with respect to the constant strain rate, s,

$$T = st, \tag{25}$$

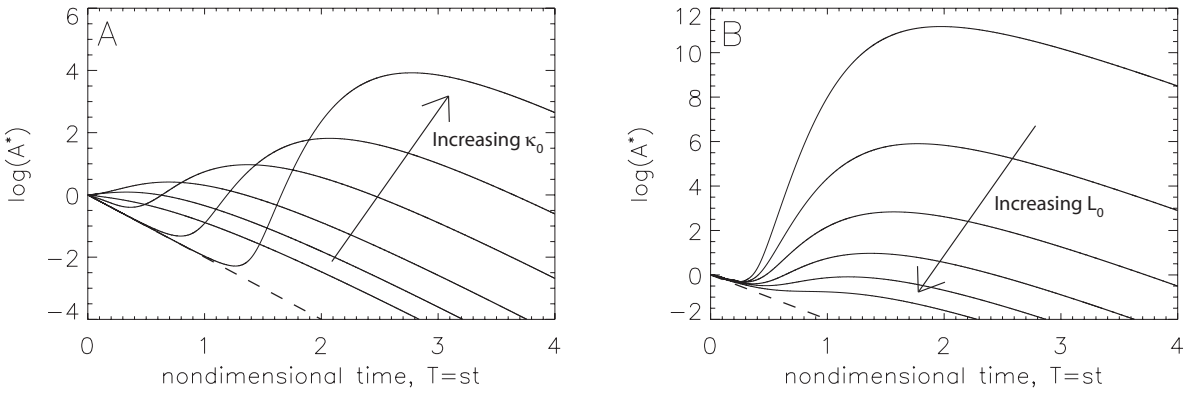

Figure 2: Evolution of $\log(\mathcal{A}^*(T))$ for various parameter values. Panel A: $L_0 = 0.8L_c$ and $\kappa_0 = \exp[-2, -1, 0, 1, 2, 3]$, as indicated. Panel B: $L_0 = 0.8L_c \exp[-1.5, -1, -0.5, 0, 0.5, 1]$ and $\kappa_0 = 1.0$, as indicated. The dashed lines show the kinematic decay $\log(\mathcal{A}^*(T)) = -2T$.

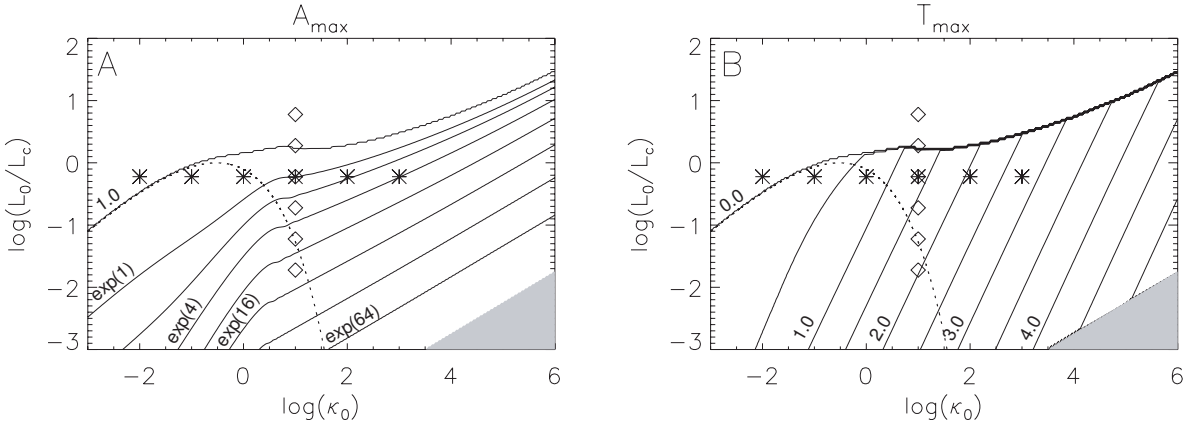

Figure 3: Panel A: Contours are $\mathcal{A}_{\max}$, the dotted line represents the boundary between positive and negative initial growth given by $I(\kappa) = 2s$ (see (23) and discussion) and the symbols indicate the parameter values used in Figure 2. Panel B: Contours are $T_{\max}$. In both plots the shading indicates regions of parameter which were not investigated.

leaving only two non-dimensional parameters in the linear equations: the initial values of L/L_c and $\kappa = kL$ which we write as L_0/L_c and $\kappa_0 = k_0 L_0$ respectively. In addition the solution depends on the initial structure of the perturbation, $\hat{\boldsymbol{\eta}}(0)$, but here we only consider the maximum amplification, $\mathcal{A}^*(t)$, introduced in (18). Recall that the wavenumber of each Fourier mode evolves according to (21) so that the full solution is

$$\boldsymbol{\eta}(x,t) = \hat{\boldsymbol{\eta}}(t)\exp(\mathrm{i}k_0 \mathrm{e}^{-st}x). \tag{26}$$

The maximum amplification, $\mathcal{A}^*(t)$, can be calculated from numerical integrations using the method of Dritschel et al. (1991) as follows. For given values of L_0 and κ_0 we numerically integrate the system just twice with different initial conditions to obtain linearly independent solutions $\hat{\boldsymbol{\mu}}(t)$ and $\hat{\boldsymbol{\nu}}(t)$. As the equations are linear, any solution $\hat{\boldsymbol{\eta}}(t)$ can be obtained from linear combinations of the form:

$$\hat{\boldsymbol{\eta}}(t) = \alpha\hat{\boldsymbol{\mu}}(t) + \beta\hat{\boldsymbol{\nu}}(t) \tag{27}$$

where α and β are complex constants. $\mathcal{A}(t)$ then takes the form

$$\mathcal{A}(t) = \mathrm{e}^{-2st}\left(|\alpha|^2|\hat{\boldsymbol{\mu}}|^2 + |\beta|^2|\hat{\boldsymbol{\nu}}|^2 + 2\mathrm{Re}(\alpha\beta^*\hat{\boldsymbol{\mu}}\cdot\hat{\boldsymbol{\nu}}^*)\right)^{\frac{1}{2}} \tag{28}$$

which can be maximised over all α and β. Choosing $\hat{\boldsymbol{\mu}}$ and $\hat{\boldsymbol{\nu}}$ to satisfy $\hat{\boldsymbol{\mu}}(0)\cdot\hat{\boldsymbol{\nu}}^*(0) = 0$ simplifies the expressions since then $|\hat{\boldsymbol{\eta}}(0)| = 1$ only requires $|\alpha|^2 + |\beta|^2 = 1$ which, combined with the phase invariance of the dynamics, means we can write

$$\alpha = \mathrm{e}^{i\gamma}\cos\delta \tag{29}$$

$$\beta = \mathrm{e}^{-i\gamma}\sin\delta \tag{30}$$

and maximise (28) with respect to the real constants γ and δ. The maximum of $\mathcal{A}$ resulting from this calculation is

$$\mathcal{A}^*(t) = \frac{e^{-2st}}{\sqrt{2}}\left[|\hat{\boldsymbol{\mu}}|^2 + |\hat{\boldsymbol{\nu}}|^2 + \left\{(|\hat{\boldsymbol{\nu}}|^2 - |\hat{\boldsymbol{\mu}}|^2)^2 + 4|\hat{\boldsymbol{\mu}}\cdot\hat{\boldsymbol{\nu}}^*|^2\right\}^{\frac{1}{2}}\right]^{\frac{1}{2}}. \tag{31}$$

To simplify the integration numerics we use alternative variables defined by $(\hat{\lambda}_1, \hat{\lambda}_2) = (\hat{\eta}_1 + \hat{\eta}_2, i(\hat{\eta}_1 - \hat{\eta}_2))/\sqrt{2}$ as then all the coefficients in (10) are real. The natural choices of $\hat{\boldsymbol{\lambda}}(0) = (1, 0)$ and $(0, 1)$ for the two linearly independent solutions correspond to

$$\hat{\boldsymbol{\mu}}(0) = \frac{1}{\sqrt{2}}(1, 1) \tag{32}$$

$$\hat{\boldsymbol{\nu}}(0) = \frac{i}{\sqrt{2}}(-1, 1) \tag{33}$$

and this is what we use.

The integration scheme used is a second order semi-implicit scheme. Accuracy is ensured by systematically reducing the time step until convergence is achieved. Integrations have been performed over a wide range of parameter space, $(L_0/L_c, \kappa_0)$, and we now discuss the results.

As an initial illustration, Figure 2 shows the evolution of $\mathcal{A}^*$ as a function of the scaled time, T, for various parameter values. Panel A shows integrations with initial filament width $L_0 = 0.8L_c$ and several initial wave numbers, κ_0. Panel B conversely shows integrations with equal initial wave numbers and a selection of L_0/L_c values. In all simulations the long time behaviour is that of decay at the kinematic rate. In some cases, however, there is intermediate growth prior to this decay. We are interested in the magnitude of this growth and as such we define $\mathcal{A}_{\max}(L_0/L_c, \kappa_0)$ as the maximum value of $\mathcal{A}^*$ achieved throughout the integration period for each pair of parameter values, $(L_0/L_c, \kappa_0)$.

Figure 3A shows $\mathcal{A}_{\max}$ computed for a wide range of $(L_0/L_c, \kappa_0)$ values and the corresponding time at which the maxima occur, that is, $T_{\max}$ such that $\mathcal{A}^*(T_{\max}) = \mathcal{A}_{\max}$, is shown in Figure 3B. Note the logarithmic scales in these plots. The parameter values of the integrations in Figure 2 are also shown on the figure, as well as the border between positive and negative initial growth predicted by (23).

There are two features of Figure 3 which we now discuss. The first, and most important, is that for all values of the initial width, L_0, there appear to be wave numbers which have large $\mathcal{A}_{\max}$ values and therefore may be unstable in the sense that nonlinear terms may

dominate the dynamics and cause the filament to 'roll-up'. The initial wave numbers, κ_0, of the perturbations which grow large increase with L_0, as expected, a result of the following combined effects: (i) the intermediate period of growth seen in Figure 2 occurs when $\kappa = O(1)$ and (ii) perturbation growth rates are larger on thinner filaments. Therefore the largest $\mathcal{A}_{\max}$ values are achieved by the largest κ_0 experiments for which the filaments are very thin by the time $\kappa = O(1)$. Note that, despite this prediction of nonlinear instability at all strain rates, an initial disturbance of any given wavenumber can be stabilised if a suitably strong strain is applied.

The second feature of Figure 3 is the small wiggle of the contours in panel A in the region of $\log \kappa_0 = 0.5$. This is near the border between positive and negative initial growth and it is associated with the non-modal transient evolution of the isolated filament case (see Section 3). In that case small scale perturbations beyond the short wave cut-off of normal mode growth exhibit oscillatory behaviour due to a lack of phase locking between the edge waves, as can be seen in Figure 8 of this paper or Figure 2b of Juckes (1995). The wiggle in Figure 3A is a manifestation of this behaviour in the straining case, although here the effect is only temporary because the short waves are stretched to a wavelength where phase locking can occur and the subsequent perturbation growth then dominates.

We now consider an alternative diagnostic from the integrations: the smallest time at which a certain threshold amplitude, $\mathcal{A}_{\rm th}$, is achieved. That is, the first $T_{\rm th}$ such that $\mathcal{A}^*(T_{\rm th}) = \mathcal{A}_{\rm th}$. The motivation for this approach is that the amplification factor $\mathcal{A}$ is a measure of the importance of nonlinear terms in the corresponding full nonlinear problem and as such filament 'roll-up' may be expected to occur when this reaches some threshold value. Without knowing this value, which will of course depend on the absolute size of the initial perturbation, we calculate our results for a range of different threshold amplitudes.

Figure 4 shows $T_{\rm th}$ for the cases $\mathcal{A}_{\rm th} = e^1 = 2.72...$ and $\mathcal{A}_{\rm th} = e^4 = 54.6....$ The plots show

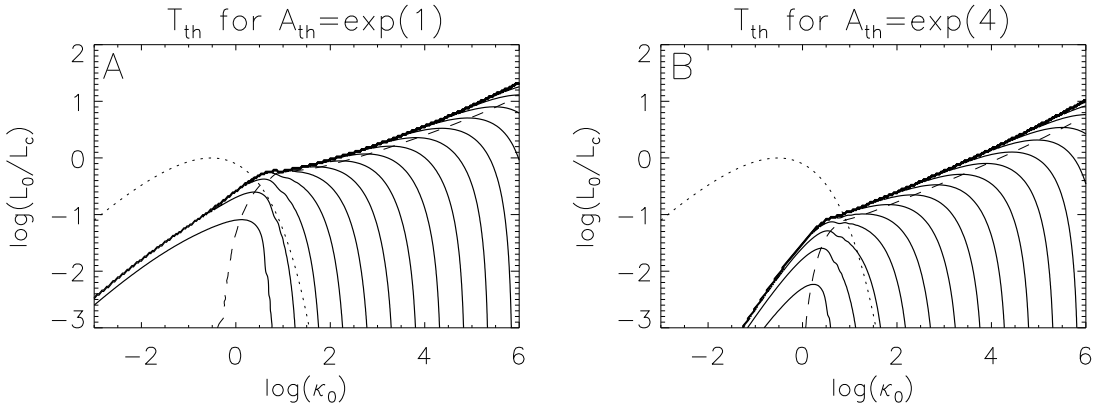

Figure 4: Contoured $T_{\rm th}$ values for threshold amplitudes $\mathcal{A}_{\rm th} = e^1$ (panel A) and $\mathcal{A}_{\rm th} = e^4$ (panel B). The dashed line indicates the minimum values, the dotted line is as in Figure 3.

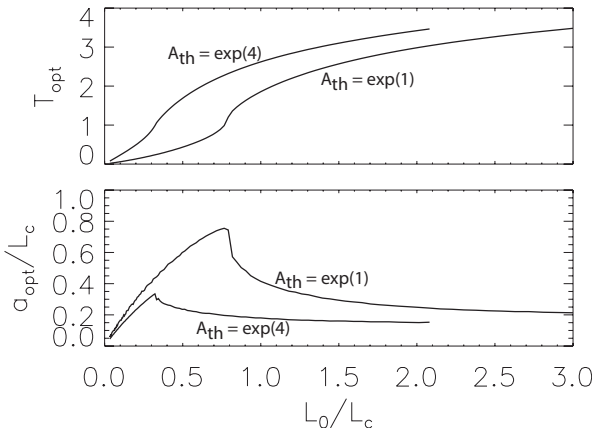

Figure 5: Upper panel: $T_{\rm opt}$ values for the threshold amplitudes $\mathcal{A}_{\rm th} = e^1$ and $\mathcal{A}_{\rm th} = e^4$. Lower panel: $a_{\rm opt}$ values for the same threshold amplitudes, see (34).

that for each L_0 there is an optimal initial wavenumber, $\kappa_{\rm opt}(L_0;\mathcal{A}_{\rm th})$, which achieves the threshold amplitude first. This is marked on the plots by the dashed lines. Figure 5A shows the corresponding optimal times, $T_{\rm opt}(L_0,\mathcal{A}_{\rm th})$, which are the times at which the optimal wavenumber perturbations reach the threshold amplitudes, as a function of L_0. As expected, the $\mathcal{A}_{\rm th}=4$ case has larger $T_{\rm opt}$ values than the $\mathcal{A}_{\rm th}=1$ case. Also shown, in Figure 5B, is an estimate of the radii of vortices formed from the instability, $a_{\rm opt}(L_0,\mathcal{A}_{th})$. This is defined such that the area of one vortex is equal to the area of filament contained within one wavelength of the optimally growing mode:

$$\pi a_{\rm opt}^2 = \frac{2\pi}{\kappa_{\rm opt}(L_0)} L_0^2. \tag{34}$$

Both panels of Figure 5 show a regime change at a certain value of L_0, which depends on the choice of $\mathcal{A}_{\rm th}$. A comparison with Figure 4 suggests the interpretation that for small L_0 values perturbations can grow immediately whereas for large values none of the initially growing perturbations reach $\mathcal{A}_{\rm th}$. Instead the first perturbation to do so is an initially decaying one which must then overcome the kinematic decay. The result is that for filaments with large L_0 values the resultant vortices are significantly smaller than the initial filament width.

6 Continued perturbations

We next consider a different approach to the problem, that of a filament under continued perturbations. By this we mean a filament which is perturbed at each instant in time during the integration. We still assume that each perturbation evolves independently of the others but expect that, since the quasi-stationary growth rate increases in time, a perturbation applied at a time $T=\tau>0$ may grow and reach the threshold amplitude $\mathcal{A}_{\rm th}$ before a perturbation applied at time $T=0$.

Note that the evolution of a perturbation applied at $T=\tau$ is equivalent to that of an initial value problem with initial value of L given by $L_0e^{-\tau}$ and therefore all the information we

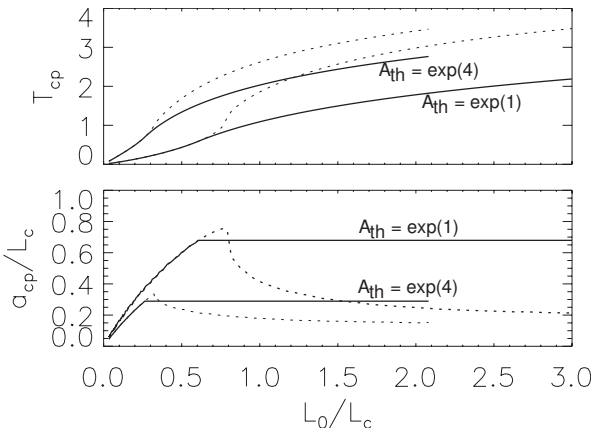

Figure 6: Upper panel: $T_{\rm cp}$ values for the threshold amplitudes $\mathcal{A}_{\rm th} = e^1$ and $\mathcal{A}_{\rm th} = e^4$ (solid lines), dashed lines are $T_{\rm opt}$ (see Figure 5). Lower panel: $a_{\rm cp}$ values for the same threshold amplitudes, see (36).

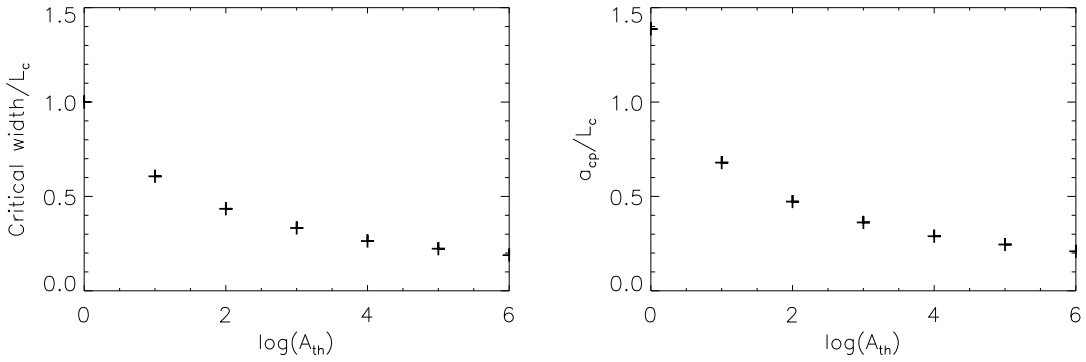

Figure 7: Panel A: Critical widths vs threshold amplitude, see text. Panel B: Resultant vortex radii vs threshold amplitude, see text.

require to test this hypothesis is included in the initial value integrations already performed.

The motivation for the continued perturbation approach comes from the fact that the wavenumber of the optimally growing modes is often very large. A filament with initial width $L = 3L_c$ has, for $\mathcal{A}_{th} = e^4$, an optimally growing mode of initial wavenumber $\kappa_0 \approx e^6$ and this appears to increase for stronger strain rates (see Figure 4). Clearly a consideration of numerical resolution or other diffusive effects may make these modes unrealistic. Further, defining the initial condition of a filament in a turbulent flow is not a well-defined procedure since there is no time $t = 0$. Instead we suppose that the perturbations are generated throughout the straining period by a noisy background velocity field.

To calculate whether a later perturbation can grow to a particular threshold amplitude before an initial perturbation consider minimising the sum of waiting until the perturbation release time τ and the subsequent optimal growth time for a filament of width $L_0 e^{-\tau}$, over all possible release times:

$$T_{cp} = \min_{\tau < T_{opt}(L_0)} \left(\tau + T_{opt}(L_0 e^{-\tau}) \right). \tag{35}$$

Either the minimising τ is zero and it is the initial perturbation which is important or else the minimising value is positive and it is a perturbation applied later which reaches the threshold amplitude first.

Figure 6A shows T_{cp} as a function of L_0 for both $\mathcal{A}_{th} = e^1$ and $\mathcal{A}_{th} = e^4$. For L_0 larger than some critical value T_{cp} is indeed smaller than T_{opt} indicating that perturbations applied later are the fastest growing. Figure 6B shows the corresponding vortex radii of the first perturbations to reach the threshold amplitude, now defined by

$$\pi a_{cp}^2 = \frac{2\pi}{\kappa_{opt}(L_0 e^{-\tau^*})} (L_0 e^{-\tau^*})^2, \tag{36}$$

where τ^* represents the minimising τ value from (35). This is constant for precisely the same L_0 values and from this we infer the following: if a filament is initially wide, in a sense made

precise below, and is continually perturbed then it has no 'memory' and will become unstable only once it has thinned to a critical width which is independent of L_0. The resultant vortices will have radii proportional to θ_0/s, again independent of how the filament was formed.

The relevant width in this statement refers to the transition in Figure 6 between the regime whereby initial perturbations dominate and the regime whereby later perturbations dominate, which depends on the value chosen for $\mathcal{A}_{\rm th}$. Figure 7A shows the critical width for various $\mathcal{A}_{\rm th}$ values, and the the resulting vortex radii are shown in Figure 7B.

Both the critical width and the vortex radii values reduce to zero for large $\mathcal{A}_{\rm th}$. For $\mathcal{A}_{\rm th} = e^4 \approx 54.6$ the theory predicts instability to occur on a wide filament once the width has reduced to $L \approx 0.3 L_{\rm c}$ and the resultant vortices to have radii $a \approx 0.3 L_{\rm c}$.

7 External shear

In this section we consider the effects of an alternative external flow field, that of a shear flow aligned with the filament as illustrated in Figure 1C. We find that such a flow can act to stabilise smooth temperature filaments in a manner to be explained, but not the discontinuous 'top-hat' profile.

The shear flow is written

$$(u_u, v_r) = r(y, 0), \tag{37}$$

where r is the rate of shear. The analysis of this case is much simpler that the strain case since the basic state does not evolve in time. The perturbation evolution is still given by (10) with a simple modification to the propagation coefficient,

$$P(\kappa) = \frac{\theta_0}{\pi L}\kappa(\log\kappa + \gamma - \log 2) - \frac{\kappa r}{2}, \tag{38}$$

which represents the modification of the local wave speed due to advection by the shear flow. The analytic solution of (14) also holds with this modification and we plot, in Figure 8, the

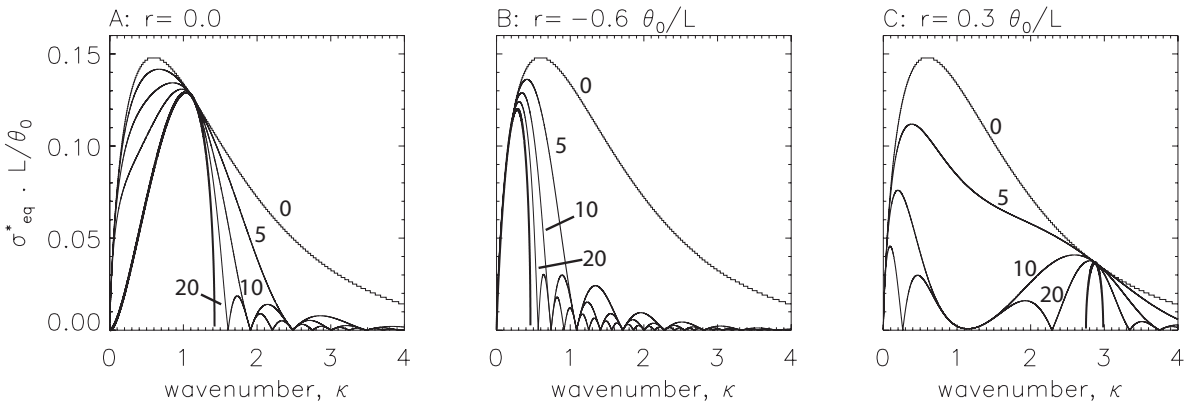

Figure 8: Equivalent growth rate values (see (19) for rates of shear $r = 0.0$ (left), $r = -0.6\theta_0/L$ (centre) and $r = 0.3\theta_0/L$ (right). The times plotted are $t = (0, 5, 10, 20)L/\theta_0$ as indicated and the bold line indicates the normal mode growth rate.

corresponding equivalent growth rates, see (19), for various shear values.

The figure shows qualitatively similar behaviour for all of the shear values. The σ^*_{eq} values are all initially equal to $I(\kappa)$ and then collapse onto the normal mode values. An adverse shear (panel C) shifts the unstable normal modes to higher wave numbers thus reducing the wavelength of the most unstable perturbations. Likewise, a complementary shear (panel B) shifts the unstable normal modes to smaller wave numbers and hence larger wavelengths. The normal mode growth rate curve always lies below the $I(\kappa)$ curve which is not affected by the shear. In contrast to the barotropic vorticity case, there is no critical shear value which stabilises the filament completely; there are always unstable modes, albeit with reduced growth rates. This can be seen from (38): for any value of r there is a κ such that $P(\kappa) = 0$, hence $\sigma = \sqrt{I^2 - P^2}$ is real.

The inability of shear to prevent normal mode growth of the SQG 'top-hat' filament is consistent with a consideration of the Fjortoft condition. Applied to this problem, the condition assures stability provided the basic state velocity profile is anti-correlated with the sign of the temperature gradients at each edge of the filament. Clearly (see Figure 1) the

velocity singularities at the filament edges prevent this from occuring for any finite shear value.

If instead we consider the case of a filament with slightly smoothed edges, however, then the singularities disappear. Suppose the filament edge is smoothed slightly over a width δL. The peak in the basic state velocity field will then scale as

$$U_{\text{peak}} \sim \frac{\theta_0}{\pi} \log(L/\delta L) \tag{39}$$

and the Fjortoft condition will be met when

$$r \sim \frac{2\theta_0}{\pi L} \log(L/\delta L). \tag{40}$$

Therefore we conclude that smooth temperature filaments can be stabilised by suitably strong shearing, the strength of which is dependent on the filament profile.

8 Conclusions

Straining and shearing tend to inhibit the development of various fluid dynamical instabilities. However, we have shown that straining is unable to stabilise temperature filaments in the surface quasi-geostrophic system since it acts to thin filaments and thus increase the instantaneous growth rates of perturbations.

Shearing is also unable to stabilise SQG 'top-hat' filaments and this is due to the velocity singularities they induce.

For the straining case our numerical integrations show that the increase in perturbation growth rate is large enough that following the evolution of a single perturbation is not the fastest way to reach large amplitude. Instead, by considering many perturbations applied continuously in time, we found that there is an optimal width for applying a perturbation such that it grows to a given threshold amplitude first. According to this simple theory, the size of the resultant vortices is independent of the previous history of the filament, instead

being proportional to θ_0/s, with θ_0 the temperature anomaly of the filament and s the strain rate.

Diffusion will act to smooth the 'top-hat' filaments studied here possibly making the method unsuitable. However, it can be shown analytically that the combined effects of straining and diffusion introduces a critical filament width

$$l_\nu = (\frac{\nu}{s})^{1/2}, \tag{41}$$

where ν is the diffusion coefficient, above which diffusion plays a minor role. We therefore expect filament instability to occur readily if $L_\mathrm{c} \gg l_\nu$, or alternatively, if filament amplitudes typically satisfy

$$\theta_0 \gg \frac{\sqrt{\nu s}}{C}, \tag{42}$$

where $C \approx 0.0742$. For filaments satisfying these criteria, diffusion can be ignored.

References

Ambaum, M. H. P. & Athanasiadis, P. J. 2007 The Response of a Uniform Horizontal Temperature Gradient to Heating. *J. Atmos. Sci.* **64**, pp. 3708–3716.

Bishop, C. H. & Thorpe, A. J. 1994 Frontal Wave Stability during Moist Deformation Frontogenesis. Part I: Linear Wave Dynamics. *J. Atmos. Sci.* **51**, pp. 852–873.

Constantin, P., Majda, A. J. & Tabak, E. 1994 Formation of strong fronts in the 2-D quasi-geostrophic thermal active scalar. *Nonlinearity* **7**, pp. 1495–1533.

Dacre, H. F. & Gray, S. L. 2006 Life-cycle simulations of shallow frontal waves and the impact of deformation strain. *Quart. J. Roy. Meteor. Soc.* **132**, pp. 2171–2190.

Dritschel, D. G. 1989 On the stabilization of a two-dimensional vortex strip by adverse shear. *J. Fluid Mech.* **206**, pp. 193–221.

Dritschel, D. G., Haynes, P., Juckes, M. & Shepherd, T. 1991 The stability of two-dimensional vorticity filament under uniform strain. *J. Fluid Mech.* **230**, pp. 647–665.

Held, I. M., Pierrehumbert, R. T., Garner, S. T. & Swanson, K. L. 1995 Surface quasi-geostrophic dynamics. *J. Fluid Mech.* **282**, pp. 1–20.

Juckes, M. 1994 Quasigeostrophic dynamics of the tropopause. *J. Atmos. Sci.* **51**, pp. 2756–2768.

Juckes, M. 1995 Instability of Surface and Upper-Tropospheric Shear Lines. *J. Atmos. Sci.* **52**, pp. 3247–3262.

Juckes, M. 1999 The structure of idealised upper-tropospheric shear lines. *J. Atmos. Sci.* **56**, pp. 2830–2845.

Lapeyre, G. & Klein, P. 2006 Dynamics of the upper oceanic layers in terms of surface quasigeostrophy theory. *J. Phys. Ocean.* **36**, pp. 165–176.

Müller, J. C., Davies, H. C. & Schär, C. 1989 An Unsung Mechanism for Frontogenesis and Cyclogenesis. *J. Atmos. Sci.* **46**, pp. 3664–3672.

Pierrehumbert, R. T., Held, I. M. & Swanson, K. L. 1994 Spectra of Local and Nonlocal Two-dimensional Turbulence. *Chaos, Solitons and Fractals* **4**, pp. 1111–1116.

Schär, C. & Davies, H. C. 1990 An Instability of Mature Cold Fronts. *J. Atmos. Sci.* **47**, pp. 929–950.

Tulloch, R. & Smith, K. S. 2006 A Theory for the atmospheric energy spectrum: Depth-limited temperature anomalies at the tropopause. *Proc. Natl. Acad. Sci. USA* **103**, pp. 690–694.